Heliyon 10 (2024) e38725

Contents lists available at ScienceDirect

Heliyon

journal homepage: www.cell.com/heliyon

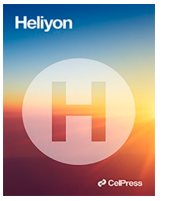

Research article

A NIRS-based recognition of coal and rock using convolution-multiview broad learning system

Yuanbo Lv [a], Shibo Wang [a,*], En Yang [b]

[a] College of Mechatronic Engineering, China University of Mining and Technology, Xuzhou, 221116, China
[b] College of Intelligent Manufacturing, Jiangsu Vocational Institute of Architectural Technology, Xuzhou, 221116, China

ARTICLE INFO

Keywords:
Coal and rock classification
Near-infrared spectrum
Improved broad learning system
Baseline correction

ABSTRACT

Achieving high production in the top coal caving process from thick coal seams is crucial. Thus, the timely decision of when to stop caving poses an urgent challenge to impact the mining loss rate and cost recovery. To address this issue, an innovative recognition system has been developed using Near-Infrared Spectroscopy (NIRS) technology. It stands out for its on-site usability, it enables rapid data collection and local recognition at the longwall face. Furthermore, to overcome the limitations of existing methods in adapting to variations in spectral data quality during on-site collection and the lack of integration of spectral data across different feature processing stages, a coal-rock recognition method has been developed which can ignore the influence of acquisition factors(granularity, light source angle, and detection sensor angle). This method incorporates the features of convolution and multi-view into the BLS model, the designed model structure exhibits a remarkable recognition accuracy of 99.78 %. The model was deployed into the recognition system, and experimental tests were conducted on the working face. The results showed that the recognition system can effectively identify the entire coal-caving process and achieve a recognition accuracy of 92.3 %. This capability is crucial for determining the optimal point to stop roof caving.

1. Introduction

The Longwall Top Coal Caving (LTCC) technology serves as a fundamental solution to address safety and production challenges during the mining of thick and extremely thick coal seams [1–5]. Referring to Fig. 1, LTCC involves five processes [6].

1. The coal wall is cut by the shearer as it travels along the front Armored Face Conveyor (AFC);
2. Hydraulics supports are pulled towards the coal wall after cutting is complete;
3. The rear AFC starts transporting coal;
4. The tail canopies swing to form a gap;
5. Top coal flows out along the gap.

The most critical task During the LTCC process is determining whether the top coal has fully caved. Typically, the completion of the LTCC is confirmed by observing the rear AFC. Based on detecting the substance type on the rear AFC, the automatic control of tail

* Corresponding author.
E-mail address: wangshb@cumt.edu.cn (S. Wang).

https://doi.org/10.1016/j.heliyon.2024.e38725
Received 3 September 2024; Received in revised form 27 September 2024; Accepted 28 September 2024
Available online 1 October 2024

canopies proves advantageous in achieving a highly satisfactory balance between recovery and rock mixing rates. However, the observation of the rear scraper is conducted in a high-noise environment, making it difficult for the time of whole top coal caving to be accurately determined through auditory or visual methods.

Currently, several methods have been explored to identify substances on the rear AFC. These methods include image recognition based on visual features [7], gamma ray recognition for detecting radioactive intensity [8,9], roof caving theory [10–12], as well as vibration and sound recognition to indirectly assess the status of hydraulic supports [13–15]. These recognition techniques fundamentally leverage distinctions in the physical characteristics of coal and rock, encompassing aspects like appearance, radiation level, density, and hardness. In diverse mining areas, variations in the types of coal and rock left behind after geological movements can significantly impact the applicability of recognition methods [16]. To address these challenges, a recognition method based on the chemical properties of coal and rock is proposed in this work. Near Infrared Spectroscopy (NIRS) emerges as a suitable solution, offering rapid composition detection and easy technology transfer.

NIRS is an analytical technique that utilizes the near-infrared region of the electromagnetic spectrum, approximately 780–2500 nm. This technique is based on the specific wavelengths of light absorption and scattering by different compounds in this region [17]. By analyzing these characteristics, NIRS can identify and quantify various chemical constituents within a sample. The basic principle of NIRS recognition is shown in Fig. 2. When light emitted from a source illuminates the material, the incident light covers a broad range of wavelengths. As the incident light interacts with the material, it undergoes reflection, refraction, and absorption, resulting in emitted light that carries information about the substance. After the emitted light, after passing through wavelength selection by a detector and Charge-Coupled Device (CCD), the emitted light is ultimately converted into a digital signal, which is then processed by a chip to complete the data analysis. Currently, NIRS has proven its efficiency in several fields, such as space [18], food [19], plants [20], and medicine [21]. Moreover, in the mining industry, researchers have used NIRS to determine coal and rock types, subtypes, geographical sources, and industrial components.

For instance, Xiao et al. [22] and He et al. [23] used a Support Vector Machine (SVM) and an Extreme Learning Machine (ELM) to distinguish between coal and rock. Moreover, Zou et al. [24] used an enhanced Mahalanobis distance-based method against outliers in the dataset. In addition, Begum et al. [25] built classic machine learning models (Logistic Regression, Random Forest, and SVM) to identify the coal subcategory. Furthermore, Principal Component Analysis (PCA) and improved Linear Discriminant Analysis (LDA) were combined by Yu et al. [26] to address the limited sample challenge in defining the geographic origin of the coal. Furthermore, Wang et al. [27] applied the strategy to regress the properties of coal (including ash, volatile matter, total moisture, inherent moisture, fixed carbon, and sulfur) after classification, contributing to an enhancement in accuracy.

Among the realm of existing identification methods, a variety of models are applied to address different challenges. The aforementioned study conducted experiments and highlighted the prevalence of SVM and LR as widely used models. These models boast a robust theoretical foundation and demonstrate versatility in handling tasks. However, they mainly handle ideal data collected under singular conditions, posing challenges in evaluating their effectiveness in identifying field spectral data. Consequently, a need arises for a model specifically tailored to handle field conditions arises.

Therefore, Broad Learning System (BLS), introduced by Chen et al. [28] in 2018, is a further improvement of the Random Vector Functional Link Neural Network (RVFLNN) model. It exhibits the characteristics of simple structure, fast parameter calculation, and scalability; thus, it has been widely used since its introduction. Moreover, Jin et al. [29] and Chen et al. [30] added regularization to the BLS technique to balance the complexity and performance of the model while improving its stability. Jin et al. [31–34] addressed the issue of overly strict and binary label supervision in traditional BLS models using label enhancement techniques. Moreover, Yang et al. [35] added convolutional calculations to BLS, enhancing the model's accuracy when processing the two-dimensional data. In addition, Li et al. [36] applied this technique to image classification and yielded good results. As for Shi et al. [37], he introduced multi-view features into BLS when modeling multi-correlated data; consequently, he enhanced the model's ability to process heterogeneous data [38]. However, existing methods focus on extracting information from single-source raw data or integrating multiple-source raw data without considering the integration of single-source data at different stages of feature extraction.

To meet the environmental requirements for LTCC, specialized equipment for on-site recognition must be designed. There are already many companies that have developed products that are adaptable to different spectral analysis needs. Buchi GmbH has created an online detection device that can be installed on conveyor belts and screw conveyors, as shown in Fig. 3(a), which uses different types of light signals, such as near-infrared and visible light, to identify the information of the tested object. Spectra Flow GmbH has developed a spectral collection and analysis device that can detect various mineral contents continuously, as shown in Fig. 3(b). This device comprises a lampshade, dust cover, light source, light source holder, spectrometer lens, optical fiber, and other parts, and this device can be used with high precision and adaptability in multiple regions. Currently, no company has designed a spectral collection

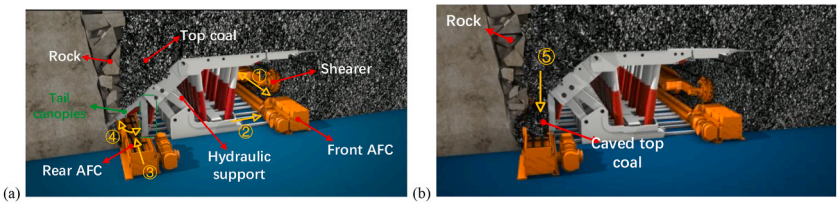

Fig. 1. (a) Schematic diagram of LTCC.

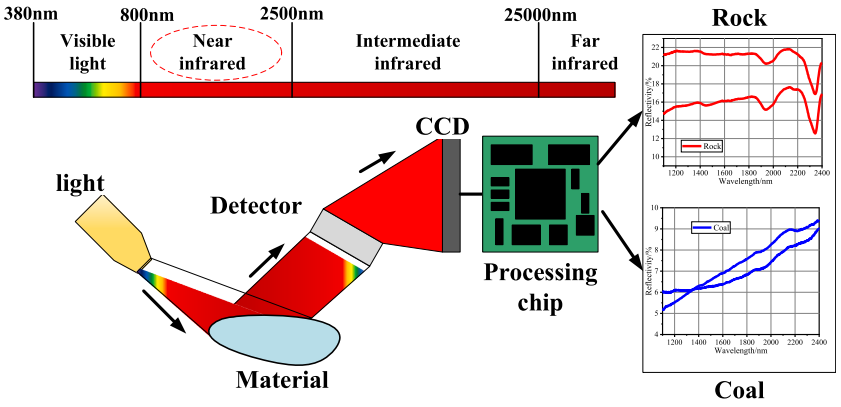

Fig. 2. Basic principle of NIRS recognition.

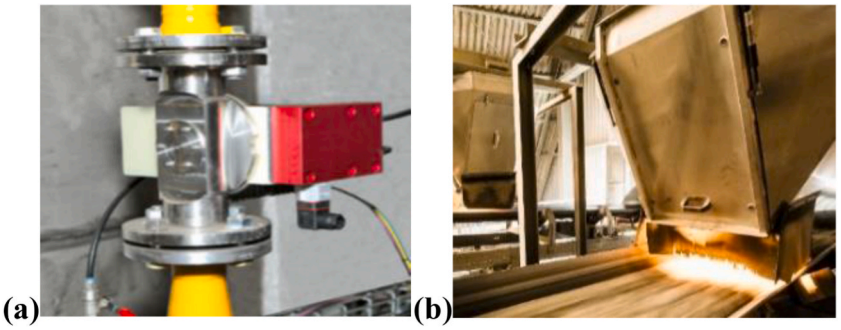

Fig. 3. (a) Buchi's online detection device and (b) Spectra flow's spectral collection and analysis device.

device that can be used underground. Therefore, it is necessary to design a coal and rock recognition device suitable for use in the LTCC process. Additionally, it is essential to develop a recognition algorithm that can adapt to the operational conditions on-site.

2. Recognition system design

2.1. Hardware design

The hardware of the recognition system is divided into two components, as illustrated in Fig. 4: the acquisition and processing parts. The processing part includes an industrial computer, a spectrometer (NIR512−2.5−HSC−EVO from Avantes, Netherlands), an optical path switcher (PLS-A from WYOPTICS, China), and a relay with a solid-state relay featuring a 24 V rated voltage. The industrial computer utilizes the UP Xtreme series development board from the Chinese company AAEON. The spectrometer boasts 512-pixel detectors, a measurement wavelength range of 1000–2500 nm, and a spectral resolution of 3.2 nm. Moreover, the PLS-A optical path switcher facilitates automatic switching between two optical paths, streamlining the calibration process for the spectrometer.

The acquisition part comprises a light source, a probe, an optical path, an optical fiber, and an air knife. The light source is a 200 W

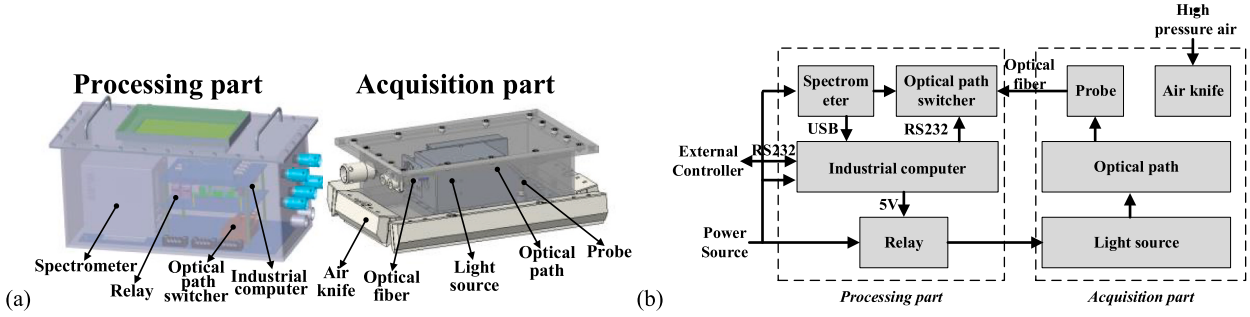

Fig. 4. 3D model(a) and schematic diagram (b) of the hardware for the coal-rock recognition system.

halogen lamp with a wavelength ranging between 350 and 2500 nm. For the probe, the W-84UV type collimator is utilized, featuring a diameter of 25 mm and a wavelength ranging between 185 and 2500 nm. The optical path channel incorporates convex lenses, concave focusing mirrors, and plane mirrors to transform the stray light emitted by the source into parallel light. This setting ensures uniform projection, resolves the problem of light source focusing, and maintains illumination intensity within the 300–900 mm distance from the object as per the requirements. Moreover, the optical fiber employed is a quartz optical fiber with a core diameter of 600 μm. The air knife, a QD-350 type product from the Chinese company Sihai, consumes 1.22 m3/min of air, establishing a relatively clean space during the collection process.

2.2. Software design

The flowchart depicted in Fig. 5 outlines the processing steps of the software module employed in this recognition system. Upon initialization, the system first checks whether spectrometer calibration is completed. If not, it switches the optical path to gather spectra in dark conditions for calibration. After calibration, it switches back and awaits operational instructions from an external controller. Upon receiving the start command, the light source is activated and initiates the collection of reflected light is initiated using the spectrometer. In the laboratory, the number of repeated measurements was set to five, and the average of the five collected spectra was taken as the final output spectrum. In field collection, the number of repetitions can be adjusted according to the movement speed of the substance being sampled; the faster the movement, the fewer repetitions.

Additionally, parameters, such as the number of integrations and integration time, during spectrum collection need to be adjusted based on the light source's brightness and the ambient light's intensity. Subsequently, a recognition model is employed for identification, and the results are transmitted back to the external controller. In the event of a stop command, the light source is deactivated. Otherwise, the system continues data collection for recognition.

3. Recognition model design

This section introduces the recognition models integrated into the recognition system, as illustrated in Fig. 6. The designed model incorporates both original and feature-processed data. Original data represents information directly obtained from the spectrometer, while the feature-processed data undergoes preprocessing and feature extraction. Following the processing by the improved BLS model, the system generates the recognition results.

3.1. Spectrum preprocessing

The spectrometer excels at data collection within the 1000–2500 nm wavelength range. However, inherent resolution limitations in the instrument yield only 512 raw data points. To mitigate information loss during subsequent processing, expanding the data set becomes necessary. Resampling proves to be a common technique for data expansion. In contrast to polynomial interpolation, which can introduce discontinuities at nodes, piecewise linear interpolation with spline interpolation performs low-order interpolations on each segment interval. This approach offers the advantages of curve smoothness and robust convergence [39]. Hence, spline interpolation is selected for data resampling process. To maintain fidelity to the original curve and minimize deviations, a smaller interpolation interval is employed, ensuring accurate tracking of the original data with reduced error. The interpolated spectral resolution is set at 0.25 nm, leading to a substantial increase in data points, culminating a final count of 6000 points in the spectral data.

To eliminate the impact of clutter caused by ambient light on the analysis, the Savitzky-Golay (SG) smoothing algorithm is applied [40]. This algorithm employs a sliding window and polynomial fitting to effectively smooth the data. The degree of smoothing is modulated by adjusting the size of the sliding window and the order of polynomial fitting within that window. The specific values for these parameters will be determined through experimental exploration in subsequent stages.

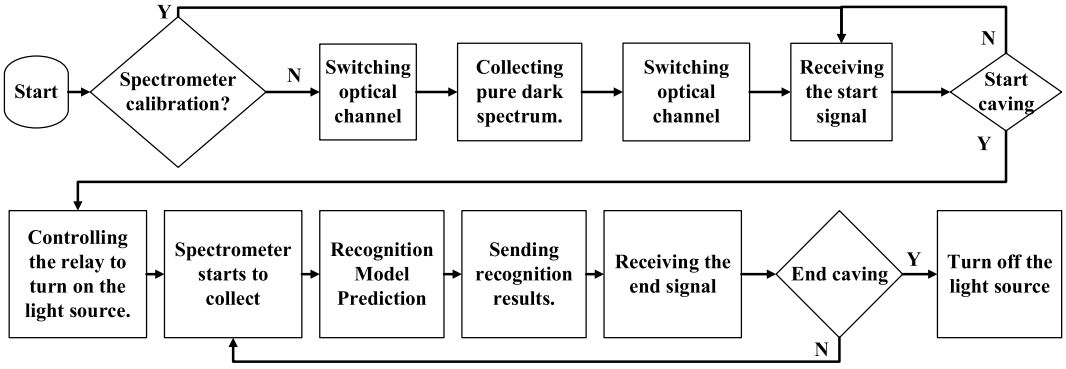

Fig. 5. Flowchart of the recognition system processing.

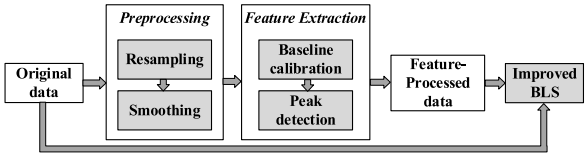

Fig. 6. Flowchart of the recognition model processing.

3.2. Feature extraction

The characteristics of coal and rock samples, encompassing surface roughness, particle size, and degree of coalification, coupled with detection conditions like the angle of the light source and the angle of the detection sensor, can include variations in the overall trend of the spectrum trend. This phenomenon, known as baseline shift, requires data calibration to mitigate its influence. In this study, calibrating many types of spectra with identical parameters is vital, emphasizing the universality of the calibration technique. To address this, asymmetrically reweighted Penalized Least Squares (arPLS) is a useful approach for estimating spectrum baselines without necessitating prior knowledge of the sample's composition, peak detection, or mathematical assumptions regarding the background noise distribution [41].

Let y a single spectral data of length 1500 having equal intervals. z is the baseline to be found, which should follow the trend of y while keeping its smoothness. A minimization function is first built:

$$S(z) = (y - z)^T (y - z) + \lambda z^T D^T D z \tag{1}$$

where $S(z)$ is the regularized least squares function, D is a difference matrix, and λ is a parameter used to adjust the balance between fitness and smoothness.

A weight vector w is then introduced. Let W be a diagonal matrix. Equation (1) can then be rewritten as:

$$S(z) = (y - z)^T W (y - z) + \lambda z^T D^T D z \tag{2}$$

The solution of the minimization problem is given by:

$$\frac{\partial S}{\partial z^T} = -2W(y - z) + 2\lambda D^T D\lambda = 0 \tag{3}$$

$$z = \left(W + \lambda D^T D\right)^{-1} W y \tag{4}$$

The following partially balanced but asymmetric weights are then chosen:

$$w_i = \begin{cases} logistic(y_i - z_i, m_{d^-}, \sigma_{d^-}), & y_i \geq z_i \\ 1, & y_i \leq z_i \end{cases} \tag{5}$$

$$logistic(d, m, \sigma) = \frac{1}{1 + e^{2(d-(-m+2\sigma))/\sigma}} \tag{6}$$

Where $d = y\text{-}z$, $d^- = \{d | y_i < z_i\}$, m_{d^-} and σ_{d^-} are respectively the mean and standard deviation of d^-, and logistic is a generalized logistic function.

Moreover, the algorithm is programmed to detect baselines positioned below the calibration data. However, the concave spectral features of coal and rock do not meet this requirement as they are located above the baseline. Thus, to tackle this challenge, a transformation of the original spectrum precedes the baseline calculation:

$$s^{\triangle} = -(\text{arPLS}((-s) + 2\bar{s}) - 2\bar{s}) \tag{7}$$

$$s^{+} = s^{\Delta} - s \tag{8}$$

where s represents the spectrum after preprocessed, $\bar{s}$ is the mean of s, arPLS is applied as the baseline correction operations, $s^{\triangle}$ is the spectrum baseline, and, finally, s^+ denotes the spectral data calculated after the baseline elimination. Therefore, Eq. (7) is used to transform concave features into convex ones, helping in improving the accuracy of the baseline fitting. As for Eq. (8), it is used to eliminate parts of the spectrum that are not relevant to the spectral features, facilitating the detection of peaks in subsequent analyses.

To perform peak detection in order to determine the position at each peak, the first derivative of the spectral data is firstly computed. Consequently, the positions where the slope changes from negative to positive are recorded. However, since the smoothing process recalls some local fluctuation features, it becomes mandatory to filter all extreme points. This is realized based on the wavelength distance, peak height, and peak width between the characteristic peaks. In such a case, the minimum wavelength distance is set between adjacent peaks to 200 nm, the minimum peak width is set to 30 nm, and the minimum peak height is set to 5. Consequently, all the peaks obtained earlier are collected and the union of the peak width collection is taken. This is achieved to accommodate characteristic widths of different spectra to the greatest extent possible. By taking the union, the peak value interval is

derived. Moreover, the peak interception is performed on the extracted spectrum, preserving only the data within the peak value interval and setting all other data to zero. The illustrative figures of the peak detection process shown in Fig. 7.

3.3. Basic BLS

Fig. 8 represents the structure of the basic BLS. In this structure, an enhancement layer is incorporated with feature layer to extract features. In addition, the output weight is computed by combining the feature layer with the enhancement layer, realizing a significant improvement in the model's performance.

Assuming that X is the input matrix having a size $N \times M$, where N represents the number of sample and M denoting the feature dimensionality. The feature layer has a groups of feature mappings, each generating k nodes. The output of feature layer Z is then calculated as follows:

$$Z = \varphi(XW_e + \beta_e) \tag{9}$$

where W_e and β_e are feature weights randomly generated and uniformly distributed, φ indicates a nonlinear activation function, and Z is represented as follows: $[Z_1, \ldots, Z_a]$. Similarly, the enhancement layer has b groups of enhancement mappings where each one generates r nodes. In addition, the output of the feature layer H is computed as follows:

$$H = \varsigma(ZW_h + \beta_h) \tag{10}$$

Hence, the broad model can be expressed as follows:

$$\begin{aligned} &Y = [\varphi(X_1 W_{e1} + \beta_{e1}), \cdots \varphi(X_a W_{ea} + \beta_{ea}) | \\ &\varsigma(Z_1 W_{h1} + \beta_h), \cdots \varsigma(Z_b W_{hb} + \beta_{hb})] W^m = [Z_1, \cdots Z_a | H_1, \cdots H_b] W^m = \left[Z^a \middle| H^b\right] W^m = A^m W^m \end{aligned} \tag{11}$$

where Y indicates the output matrix of size $N \times C$, C is the output feature dimensionality, symbol $|$ implies the matrix concatenation operation, ς represents a nonlinear activation function, and W^m denotes the output weight which can be easily computed through the ridge regression approximation:

$$\underset{W^m}{\operatorname{argmin}} : \|A^m W^m - Y\|_2^2 + \lambda \|W^m\|_2^2 \tag{12}$$

where λ denotes the constraints on the sum of the squared weights. The output weights can then be computed as follows:

$$W^m = \left(\lambda I + A^m A^{mT}\right)^{-1} A^{mT} Y \tag{13}$$

3.4. Improved BLS

Fig. 9 displays the structure of the improved BLS, which consists of simultaneous integration of convolution and multi-view features. The main purpose of convolution consists of extracting correlation features between wavelengths, and to compare them to fully connected layers. Moreover, it can effectively reduce the number of model parameters. On the other hand, multi-view compensates for information damage caused by the spectral processing. The detailed procedure is defined as follows:

The network processes feature-enhanced data s^+ and original data s simultaneously, using two different spectrum "perspectives". Moreover, it concatenates the feature mappings gathered from all the views to create an enhancement layer. Finally, this network combines the feature and enhancement layers to generate the output. Therefore, Convolution-Multiview BLS (C-MvBLS) represents the improved BLS and will be referred accordingly in this paper.

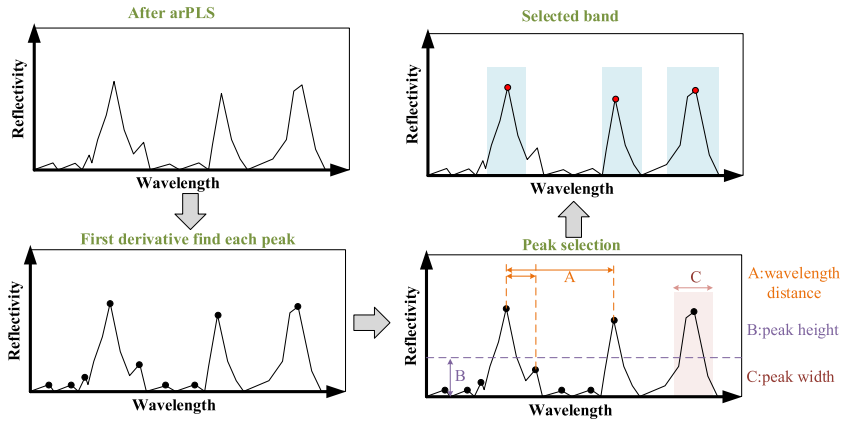

Fig. 7. Illustrative figures of the peak detection process.

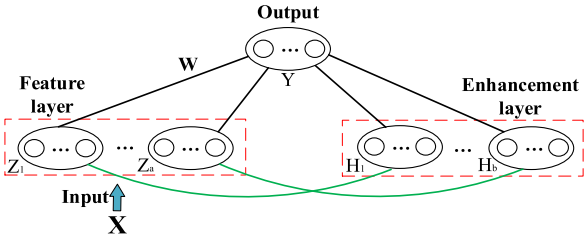

Fig. 8. Structure of basic BLS.

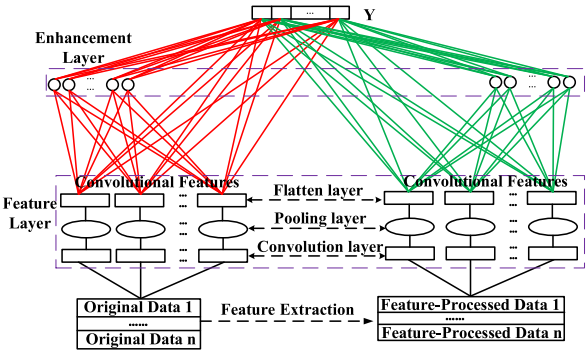

Fig. 9. Structure of the improved BLS.

Assuming that $X^p \in \mathbb{R}^{N\times M_1}$ represents the feature-processed data and $X^o \in \mathbb{R}^{N\times M_2}$ designates the original data, the feature layer output Z_v is then computed as follows:

$$\begin{aligned} Z_v &= [\max\{\eta(\mathrm{Conv}(X^p))(i'), i \le i' \le i+u\} \\ &|\max\{\eta(\mathrm{Conv}(X^o))(i'), i \le i' \le i+u\}] = [Z^p|Z^o] \end{aligned} \tag{14}$$

where *Conv* indicates the 1D convolution operator, η represents a nonlinear activation function, max is the pooling operator which merges nearby feature values into an individual one using the max pooling operator, u is the pooling kernel size, and, finally, Z^p and Z^o represents the feature layer outputs for both views. The enhancement layer output H_v is then computed as follows:

$$\begin{aligned} H_v &= \left[Z^p W_{hp} + \beta_{hp} \middle| Z^o W_{ho} + \beta_{ho}\right] \\ &= [H^p|H^o] \end{aligned} \tag{15}$$

where W_{hp}, W_{ho}, β_{hp}, and β_{ho} are randomly generated weights, whereas H^p and H^o are enhancement layer outputs for two views. Let $A_v = [Z_v|H_v]$, the final mathematical equation for the output Y_v is expressed as follows:

$$Y_v = A_v W_v \tag{16}$$

where the output weights W_v are then computed as represented here below:

$$W_v = \left(\lambda I + A_v {A_v}^T\right)^{-1} {A_v}^T Y_v \tag{17}$$

Algorithm Convolution-Multiview Board Learning System:

Input: feature-processed data $\mathbf{X^P}$, original data $\mathbf{X^O}$
Output: output weights $\mathbf{W}$
Initialization: convolution kernel size $\mathbf{k^P}$,$\mathbf{k^O}$; convolution stride $\mathbf{s^P}$,$\mathbf{s^O}$; pooling kernel size $\mathbf{u^P}$,$\mathbf{u^O}$; pooling stride $\mathbf{h^P}$,$\mathbf{h^O}$; nodes in the enhancement layer $\mathbf{n}$
Calculate $\mathbf{Z^P} = \max\{\eta(\mathrm{Conv}(\mathbf{X^P};\mathbf{k^P},\mathbf{s^P}));\mathbf{u^P},\mathbf{h^P}\}$;
Calculate $\mathbf{Z^O} = \max\{\eta(\mathrm{Conv}(\mathbf{X^O};\mathbf{k^O},\mathbf{s^O}));\mathbf{u^O},\mathbf{h^O}\}$;
Set the feature layer output $\mathbf{Z_v} = [\mathbf{Z^P}|\mathbf{Z^O}]$;
Random enhance layer weights $\mathbf{W_{hp}}$, $\mathbf{W_{ho}}$; biases $\boldsymbol{\beta}_{\mathbf{hp}}$, $\boldsymbol{\beta}_{\mathbf{ho}}$;
Calculate $\mathbf{H^P} = \mathbf{Z^P}\,\mathbf{W_{hp}} + \boldsymbol{\beta}_{\mathbf{hp}}$;
Calculate $\mathbf{H^O} = \mathbf{Z^O}\,\mathbf{W_{ho}} + \boldsymbol{\beta}_{\mathbf{ho}}$;
Set the enhance layer output $\mathbf{H_v} = [\mathbf{H^P}|\mathbf{H^O}]$;
Set the output layer's input $\mathbf{A_v} = [\mathbf{Z_v}|\mathbf{H_v}]$;
Specify squared weights λ
Calculate $\mathbf{W_v} = (\lambda\mathbf{I} + \mathbf{A_v}\mathbf{A_v^T})^{-1}\mathbf{A_v^T}\mathbf{Y_v}$
Set $\mathbf{W} = \mathbf{W_v}$

4. Materials and experiments

4.1. Sample preparation

Table 1 gathers the coal and rock samples collected from different coal mines in China, each coal and rock sample are a large block. 11 types of rock, with No. 01–11, are gathered. They belong to the three base types of sedimentary rocks: shale, sandstone, and limestone. Moreover, there are 11 kinds of coal, numbered from. 12–22, belonging to the three base types, mainly anthracite, bituminous coal, and lignite. For instance, Graham [42] and Wang [43] demonstrated through experiments that the surface roughness can affect the spectral contrast. In contrast, the particle size can influence the reflectivity and absorption characteristics of the spectra. Therefore, each kind of coal and rock sample was processed into three physical forms (blocks with nature rough surface, blocks with smooth surface, and particles with nine different diameters (8000, 4750, 2500, 1000, 500, 210, 100, 74, and 45 μm), Thus, a total of 22 * 11 subsamples were obtained, resulting in 242 subsamples. The specific block samples are large enough so that the detection range of the probe is centralized in a single block sample.

4.2. Laboratory spectrum acquisition

The platform shown in Fig. 10 is used to acquire the spectrum. Each sample has a distinct granularities and type and it is placed on stage, using a probe to collect the reflected light. The light source angle, located between the light source and the z-axis, has nine different angles (10°, 20°, 30°, 40°, 45°, 50°, 60°, 70°, and 80°). As for the detection angle θo between the detection sensor and the z-axis, it has eight different angles (10°, 20°, 30°, 40°, 50°, 60°, 70°, and 80°). These angles can comprehensively cover the possible situations that may arise during data collection. Moreover, the light source is capable to illuminate the sample from different angles. As for the detecting sensor, it collects the reflected light from different angles. Moreover, the average of the three spectra acquired for each circumstance acts as the final spectrum.

Referring to Fig. 11(a) and (b), the spectrum of coal and rock block samples are visualized respectively. It is noticeable that some types of rock, like *siltstone2*, *black shale2*, and *argillaceous limestone1*, have similar morphologies to coal. However, other researchers have shown unique absorption features differing from the coal in morphology at 1,411, 1,922, and 2204 nm. Additionally, the same type of material, such as *argillaceous limestone 1* and *2* significantly varies its slope and absorption features. Moreover, due to the lack of absorption features in the coal spectrum, all coal spectra have a high similarity degree.

As for Fig. 11(c), (d), and (e), it displays the various conditions of *argillaceous limestone 2*, including granularity, light source angle, and detection angle. The absorption feature's shape, the slope, and the reflectivity are primarily affected by the particle sizes. For instance, a diameter of 0.074 mm in the absorption feature significantly reduces the slope and increases the reflectivity. These results are consistent with those published in Ref. [44]. The light source angle affects the absorption feature depth as well as the reflectivity of the spectrum. Under an angle of 60°, the absorption feature is barely visible, and the reflectivity drops sharply. Furthermore, the detection angle has a minor impact on the spectrum, yet it affects the reflectance.

4.3. Field spectrum acquisition

The schematic diagram of the field testing with the recognition system was illustrated in Fig. 12. Field testing occurred in a mining area located in Shanxi Province, China. As soon as the hydraulic support is launched, the equipment collects spectral data and saves it until the rock is continuously observed on the rear AFC. The whole top coal caving process in this experiment lasts for approximately 19 min and 48 s, during which 834 spectral data are collected. To clearly demonstrate the complete top coal caving process, 26 spectral data points are selected from the available dataset. They are found to be reflective for different stages in the process, as illustrated in Fig. 13. The coal and rock occur at different heights, and their occurrence frequency is uneven. This fact highlights the difficulty of identifying coal and rock through LTCC.

4.4. System evaluation indicators

The laboratory and on-site spectral data gathered are applied for two-classification techniques using the proposed C-MvBLS model, having as objective to distinguish the "class" column in Table 1. The effectiveness of the model's recognition is assessed by three indicators: True Positive Rate (TPR), True Negative Rate (TNR), and Mean Efficiency (ME).

$$TPR = \frac{TP}{TP + FN} \times 100 \tag{18}$$

$$TNR = \frac{TN}{TN + FP} \times 100 \tag{19}$$

$$ME = \sqrt{TPR \times TNR} \tag{20}$$

Table 1
Types of coal and rock samples.

NO	Class	Base type	Type	Area	Mining	NO	Class	Base type	Type	Area	Mining
01	Rock	Limestone	Argillaceous limestone 1	Shandong	Xinglongzhuang	12	Coal	Anthracite	Anthracite	Ningxia	Ruqigou
02			Argillaceous limestone 2	Shandong	Xinglongzhuang	13		Bituminous coal	Lean coal	Shandong	Dongfeng
03			Clay	Shanxi	Malan	14			Meager lean coal	Shandong	Dongfeng
04		Sandstone	Siltstone 1	Shanxi	Malan	15			Meager coal	Shandong	Gaocun
05			Siltstone 2	Shandong	Xinglongzhuang	16			Coking coal	Shanxi	Malan
06			Fine sandstone	Shandong	Dongfeng	17			Fat coal	Shandong	Caozhuang
07			Medium-grained sandstone	Shandong	Dongfeng	18			1/3 coking coal	Shandong	Bayi
08		Shale	Black shale 2	Shanxi	Xinjing	19			Gas-fat coal	Shandong	Maozhuang
09			Black shale 1	Shanxi	Malan	20			Gas coal	Shandong	Xinglongzhuang
10			Sandy shale 1	Shandong	Dongfeng	21		Lignite	Lignite1	Shandong	Wutu
11			Sandy shale 2	Shandong	Xinglongzhuang	22			Lignite2	Jilin	Shulan

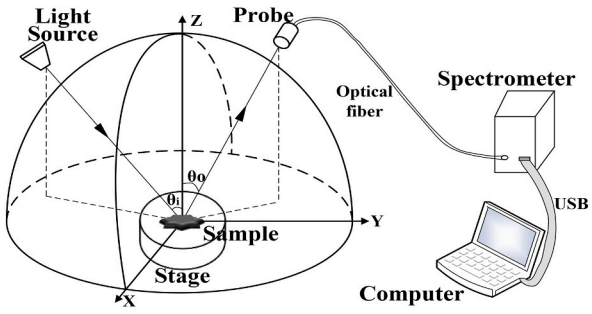

Fig. 10. Schematic diagram of the spectrum acquisition platform.

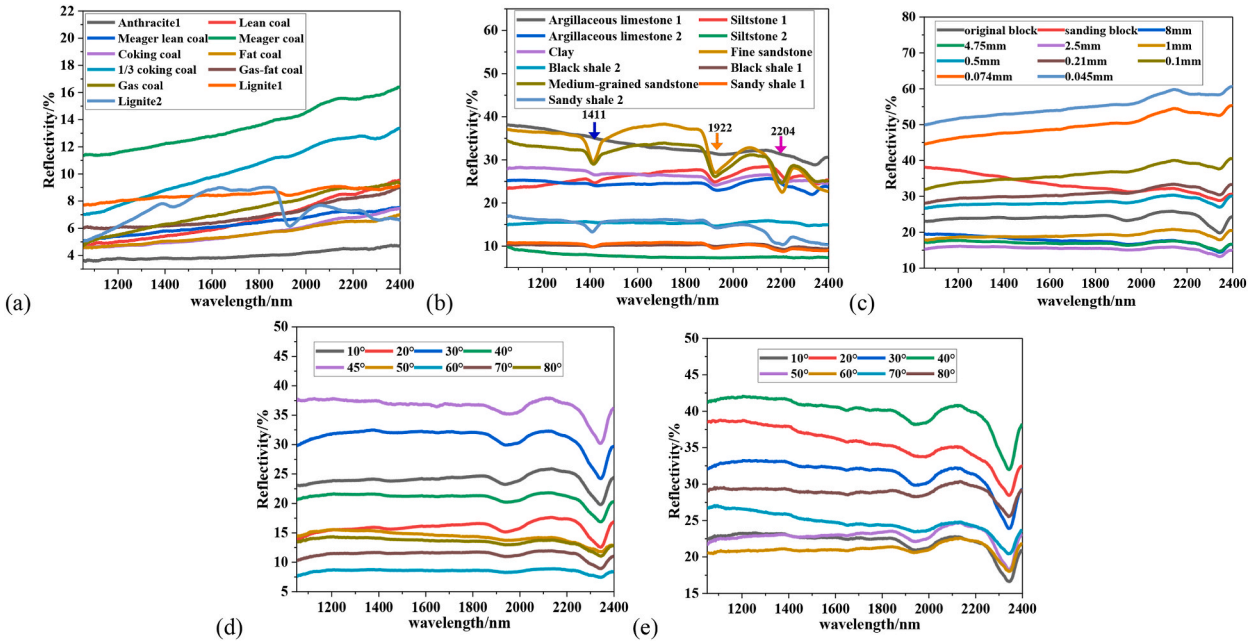

Fig. 11. Spectrum of coal/rock acquisitioned under different conditions (a) block coal, $\theta i = \theta o = 0$ (b) block rock, $\theta i = \theta o = 0$ (c) different granularities $\theta i = \theta o = 0$ (d) different light source angles $\theta o = 0$ (e) different detection angles $\theta i = 0$.

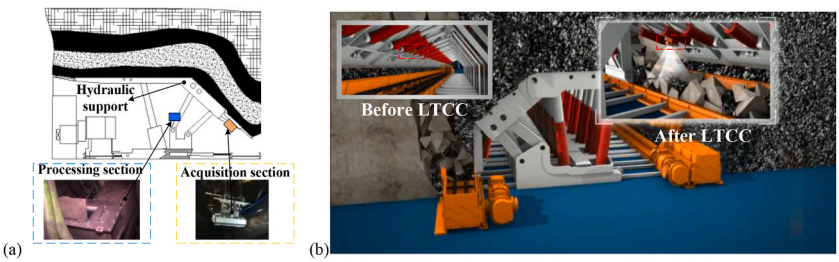

Fig. 12. Schematic diagram of the (a) field testing with the recognition system and (b) before and after LTCC process.

Referring to Fig. 14, where P and N represent, respectively, the coal and rock whereas T and F indicate, respectively, the correct and false recognition. Moreover, TPR reflects the recognition effect of certain types, TNR denotes the recognition effect of non-certain types, and, finally, ME indicates a comprehensive evaluation index.

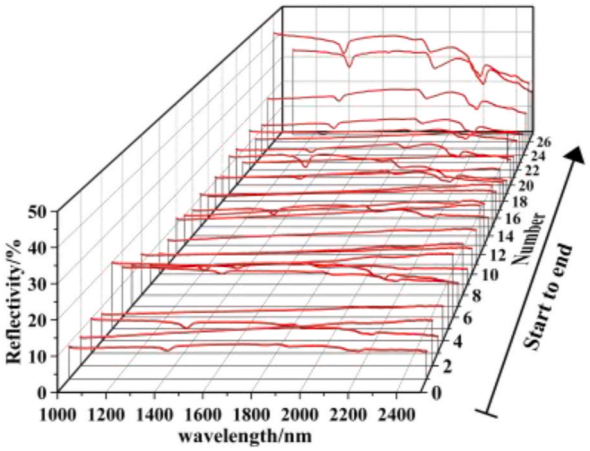

Fig. 13. Spectrum of coal/rock collected in field.

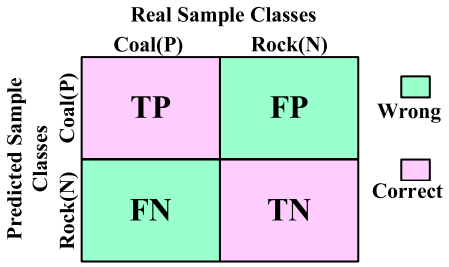

Fig. 14. Position diagram of evaluation metrics in the confusion matrix.

5. Results and discussion

5.1. Comparison of preprocessing

Five random samples were selected from the spectral data collected in the laboratory. In more detail, Fig. 15 displays the spectral curves after applying the SG smoothing technique using different parameters, such as window lengths (*wl*) and polynomial orders (*or*), regarding the spectral data. The results show that a lower order produces a slight deviation from the original trend, while a second order produces the best smoothing effect. However, a third order does not enhance the output. Reducing the window size when the order is the same will lead to worse results as data will start to fluctuate. Moreover, increasing the window size beyond a certain point will not yield in any adjustment on the results. Therefore, the adopted preprocessing scheme involves firstly the use of spline curve

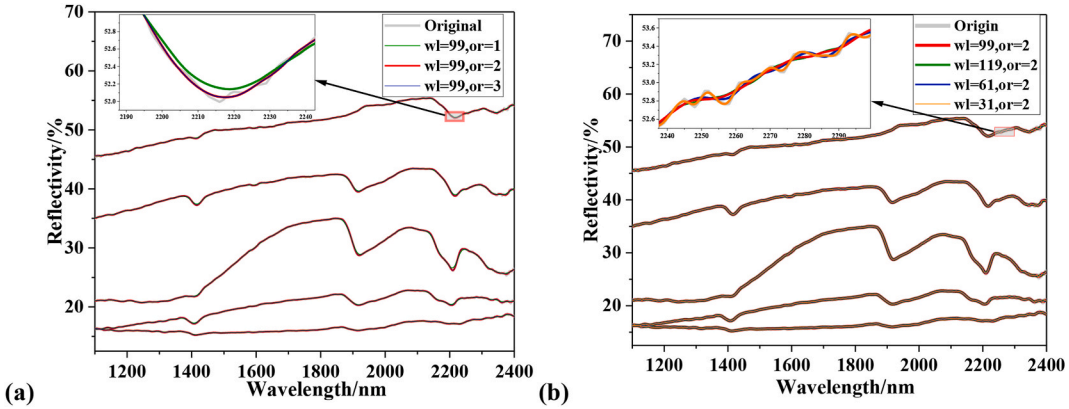

Fig. 15. Comparing different SG parameters for (a) window length and (b) order.

resampling, followed by SG smoothing with a window size of 99 and an order of two.

In order to extract specific spectral bands that distinguish between coal and rock in spectral data, the arPLS method is deployed to search for the baseline of the spectral curve, as represented in Fig. 16(a). This method subtracts the smoothed data from the baseline to effectively eliminate irrelevant band information. After baseline correction, the peak detection is applied to calculate the center positions and widths of each peak. These positions are then extracted from the corrected data to generate the two feature bands data, as shown in Fig. 16(b). This approach can retain the coal-rock differentiation information and accurately separate feature bands for different spectral data shapes; thus, it saves the computational resources for subsequent processing.

To verify the effectiveness of coal-rock classification after the extraction of the feature bands, the PCA method is used to extract the main information from the raw and feature data. For easier presentation, the top two important data components are selected from each dataset and they are plotted as a 2D distribution figure, where the shaded areas represent regions with relatively high scatter point density. Referring to Fig. 17(a), it can be observed that the feature points of the coal and rock are not distributed in a cross-manner in space. However, only the first feature shows a difference, while the other ones do not contribute to the classification task. After performing the feature extraction as presented in Fig. 17(b), the coal's features are more concentrated and less likely to mix with the rock feature points in space.

As presented in Fig. 18, the Pearson correlation coefficient method is applied to calculate the correlation between spectra of argillaceous limestone 2 under different influencing factors. Its value ranges from −1 to 1. The formula to calculate the Pearson correlation coefficient is:

$$r = \frac{\sum_{i=1}^{n}(x_i - x')(y_i - y')}{\sqrt{\sum_{i=1}^{n}(x_i - x')^2 \sum_{i=1}^{n}(y_i - y')^2}} \tag{21}$$

Where r is the Pearson correlation coefficient, n is the number of data points, x_i and y_i are the values of the two variables for the i-th data point, x' and y' are the mean of variable x and y. $r = 1$ indicates a perfect positive linear correlation, $r = -1$ indicates a perfect negative linear correlation, $r = 0$ indicates no linear correlation. Therefore, the Pearson correlation coefficient between spectral curves obtained under different influencing factors should be as close to 1 as possible. This reduces the impact of external factors such as collection conditions on the recognition process, ensuring that the same type of coal and rock exhibits similar features under different conditions, thereby reducing the difficulty of model training.

When influencing factors change, as shown in Fig. 18(a)–(c), spectral correlation can decrease or even become negative. Therefore, the relationship between spectral curves can be affected by several factors. For instance, in Fig. 11(c), the overall trend of the 2.5 mm spectrum is relatively flat, while the reflectance remains within a small range, and the absorption peak is relatively small. As a result, as shown in Fig. 18 (a), the correlation between the spectrum at 2.5 mm and larger particle sizes is notably low across various granularities. The spectrum at larger particle sizes exhibits a slight upward trend, and the degree of fluctuation is more pronounced. As shown in Fig. 18(d)–(f), following baseline correction, the correlation among the spectra for all parameters show a significant improvement, reaching a minimum correlation value of 0.8. The reason is that after baseline correction, the spectral data retains only the characteristic parts, as shown in Fig. 16(b).

However, the Pearson correlation coefficient calculation on the baseline-corrected spectral data can be misleading, because the corrected spectra often contain values near zero in specific wavelength regions, such as 1100–1350 nm, 1500–1850 nm, 2080–2120 nm, and 2300–2400 nm in Fig. 16(b). These near-zero values significantly contribute to the overall similarity but do not provide any useful features for recognition. Therefore, band selection is necessary. It is possible that after band section, the absorption peak features persist, leading to a more unified spectral curves for similar components. As shown in Fig. 18(g)–(i), while the similarity of the spectra may slightly decrease compared to after baseline correction, it does not result in a negative correlation and still maintains a decent clustering effect.

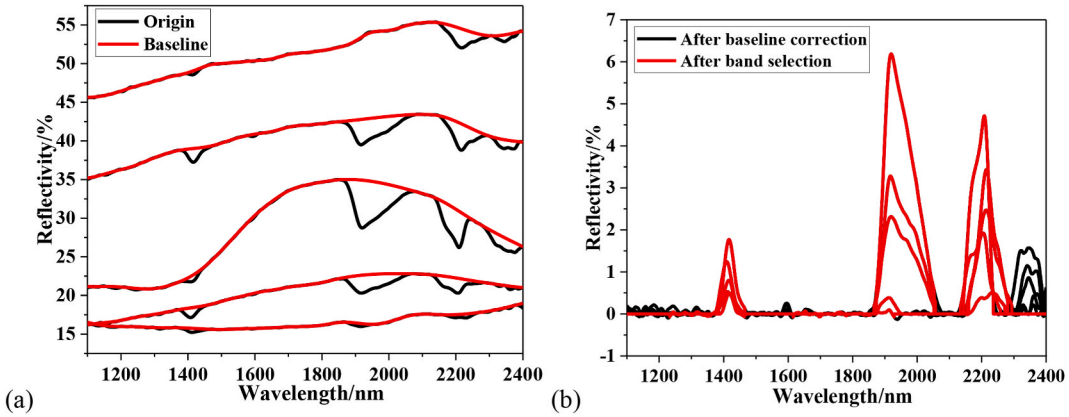

Fig. 16. Feature extraction results of baselines search (a) and band selection (b).

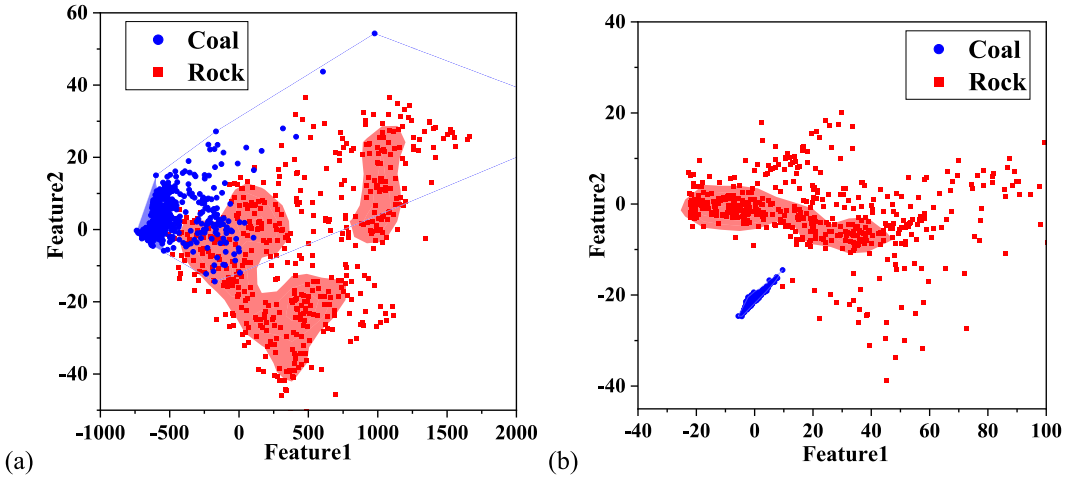

Fig. 17. 2D feature distribution of the original (a) and feature-extracted (b) spectral data.

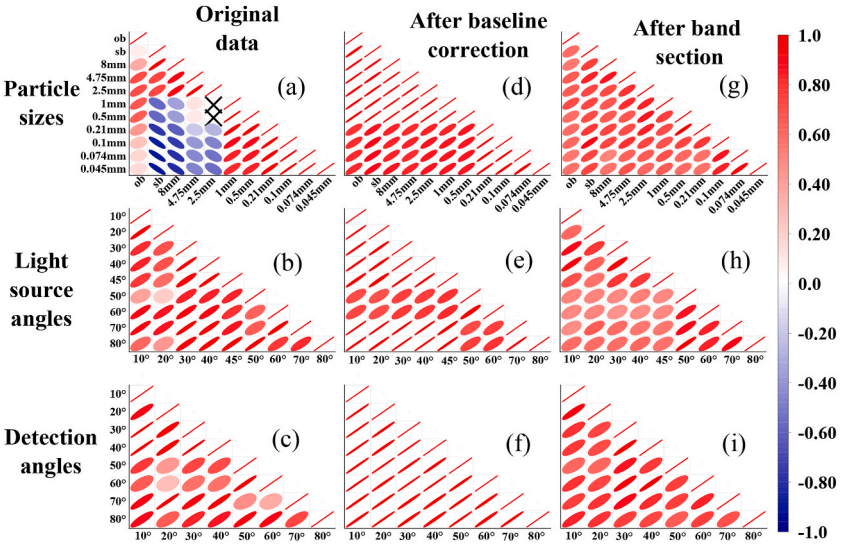

Fig. 18. Comparing the Pearson correlation coefficient between spectra under different influencing factors (particle sizes, light source angles, detection angles) after different processing stages (original data, after baseline calibration, after band selection) (significance level: 0.05).

5.2. *Comparison of structural*

To demonstrate the superior performance of the proposed C-MvBLS model, it is compared to BLS, CNN, C-BLS, and Mv-BLS models while considering similar structures. BLS refers to a basic model that has been explained in detail earlier. Moreover, CNN is a neural network model that employs convolution, pooling, and other operations to extract the required features. In addition, C-BLS replaces the linear mapping of the feature layer and the enhancement layer of the basic BLS with convolutional layers. Finally, Mv-BLS increases the number of feature layers in the basic BLS and maps distinct input data. Furthermore, three types of input data are used: original data ("*or*"), feature-processed data ("*pro*"), and the union of both ("*or* + *pro*").

Table 2
Hyperparameter list of C-MvBLS.

Hyperparameter	Range or Value	Hyperparameter	Range or Value
Convolution kernel size	[20,30]	Atride kernel size	[10,26]
Convolution kernel number	[6,11]	Feature layer group number	5
Activation function	{Relu, Sigmod}	Enhance layer group number	10
Pooling kernel size	[2,7]	Number of each group	150

In this study, a dataset of 10,496 laboratory-collected spectra was used (dataset have been deposited into the Zenodo, DOI: 10.5281/zenodo.8201508), divided into 90 % for training, 5 % for testing, and 5 % for validation. Table 2 provides the hyperparameters deployed in the C-MvBLS model where the parameters for the convolutional layer were randomly selected within a given range. When applying the model structure ablation, relevant hyperparameters were kept unchanged. To avoid the repetition of data used for training and testing, it was randomly selected from the shuffled dataset for each iteration. Additionally, each model underwent five training and prediction cycles to ensure accuracy.

Referring to Fig. 19, one can see how the accuracy and time consumption of the different structures vary. The horizontal axis displays the names of the various input data as well as the model structures. When applying single-view models, two options are available: just using the original data or just using the feature-processed data. According to Fig, 19(a), referring to the model that uses only raw data, it is observed that, in terms of TNR, CNN is more accurate in recognizing rocks compared to BLS; however, it is less accurate in recognizing coal in terms of TPR. On the other hand, C-BLS has higher recognition accuracy for both coal and rocks. The poor performance of or-BLS is attributed to its ability to handle global information but insufficient feature extraction from the original data. The or-CNN performed poorly because it only captured local features between wavelengths and lacked more layers to capture global information. The or-C-BLS, on the other hand, combined the advantages of both, integrating local and global information to achieve higher recognition accuracy. These findings indicate that adding convolutional operations to BLS can improve the model's recognition performance.

The model that employs only feature-processed data demonstrate that BLS has the highest overall recognition accuracy (ME). However, the low overall recognition accuracy of C-BLS and CNN is due to the relatively limited TPR in recognizing coal. This is mainly due to the spectral processing process that disrupts the correlation information between wavelengths. Comparing the performance of the same structured models with different inputs, both BLS and CNN show significantly improved at the level of TPR in recognizing coal after inserting feature-processed data. Thus, the compensation for the overall low recognition accuracy is achieved. Moreover, this result proves that feature-processed data improves the recognition accuracy of coal.

Comparing the performance of similar structured models exposed to single-view and multi-view settings, it can be observed that the application of MvBLS with multiple views results in higher recognition accuracy compared to the use of two single-view BLS models. This makes the recognition accuracy of coal (TPR) close to that of rocks (TNR). Moreover, the findings prove that adding multiple views in BLS can enhance the recognition performance of the model.

When comparing the proposed model C-MvBLS to other models, it has significant advantages in all three indicators, and the fluctuation range of recognition accuracy is also greatly reduced. Moreover, each training achieves stable and high-precision recognition accuracy. This result demonstrates that the proposed C-MvBLS model integrates the advantageous effects of other models and exhibits higher superiority in coal and rock recognition.

To further evaluate the real-time performance of the models when operating under recognition systems, the running time of these eight models in recognizing individual spectral data is measured. As shown in Fig. 19(b), C-MvBLS has a significantly longer running time compared to other models. However, the recognition time of the model is still measured in milliseconds, where C-MvBLS does not exceeding 200 ms. Therefore, this does not impact the real-time performance of the recognition system.

5.3. Comparison of algorithms

To demonstrate the superiority of our proposed C-MvBLS model over existing recognition models, we compare it to three commonly used models: Logistic Regression (LR), Support Vector Machines (SVM), and Random Forest (RF). The first is characterized by a low-complexity linear regression analysis model and it is often used as a classifier. SVM maps features to high-dimensional space, making it easier to distinguish characteristics. Finally, RF is an integrated learning algorithm establishing multiple decision trees to obtain a comprehensive judgment as the output result.

We apply the same dataset and data partition method as in the previous section to train the models. Table 3 demonstrates the hyperparameters used in the comparative models. During each iteration, data is randomly selected from the shuffled dataset, and each model undergoes five training and prediction cycles.

The accuracy and time consumption results for the different algorithms are presented in Fig. 20. In more detail, Fig. 20(a) shows that the LR and RF models are specific in recognizing rocks and coal, achieving higher accuracy in identifying them. However, both models have relatively lower accuracy while recognizing other categories. The recognition stability over the five training and prediction cycles is also poor for these models. However, the SVM model performs better than the LR and RF models in terms of the ME metric since it generates good recognition performance for both coal and rocks yielding in a minimal difference. On the other hand, the C-MvBLS model reaches the best recognition performance and exhibits the highest stability over the five training and prediction cycles. Its recognition indicators are the highest among the four models, approving the superiority of the proposed recognition model over the existing models.

Moreover, in Fig. 20(b), the average recognition times for LR, SVM, and RF models are all within 30 ms, showing no significant difference among them. However, the C-MvBLS model has an average recognition time of 163 ms, which is much longer than the other models. Nevertheless, this extra time consumption during the coal feeding process would not affect the real-time nature of recognition.

5.4. Comparison of data source

The drilling results presented in Table 4 illustrate the distribution of coal and rock within the roof strata. The index numbers denote distances from the working face, with higher numbers signifying greater distance. The findings underscore the prevalence of coal-rock

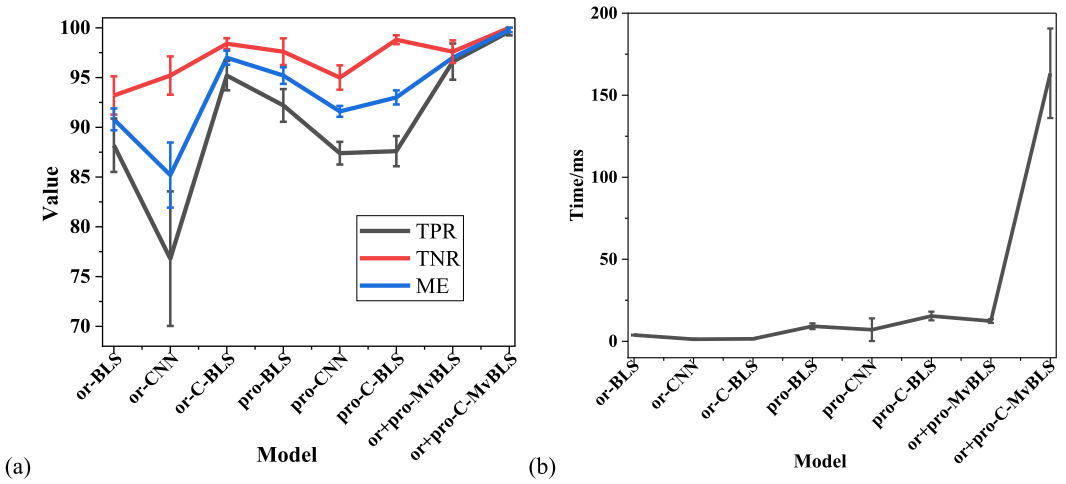

Fig. 19. Variation of accuracy (a) and consuming time(b) of different structural.

Table 3
Hyperparameter list of model for comparison.

Model	Hyperparameter	Value
LR	Penalty	0.2
	Solver	Saga
SVM	Kernel	RBF
	Penalty	10
	Gamma	1/(features size)
RF	max_depth	3
	estimators	100

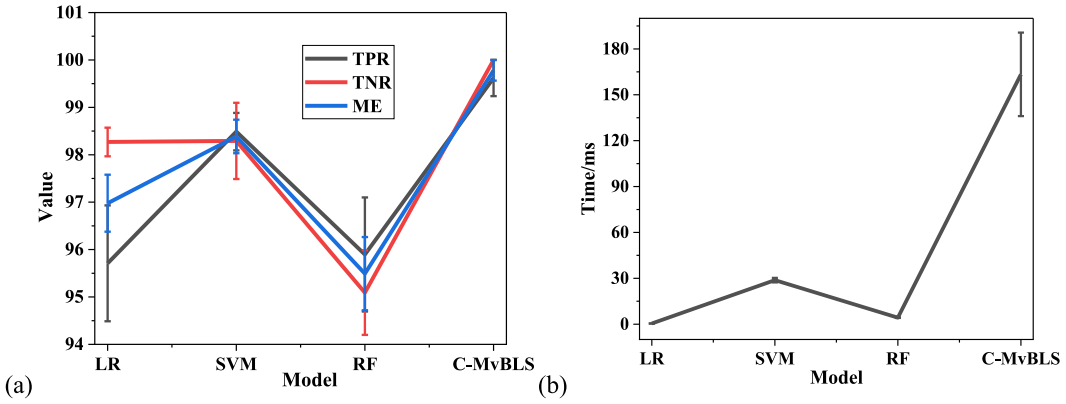

Fig. 20. Variation of accuracy (a) and consuming time(b) of different algorithms.

mixes in the top coal seam. Consequently, a recognition system with both high accuracy and real-time capabilities becomes imperative. High accuracy ensures that the material type is precisely identified, while real-time capabilities guarantee that interbedded layers are detected promptly.

The collected spectral data (as shown in Fig. 13) was used for recognition using the proposed C-MvBLS model. The final recognition results were compared to the actual field results, and the accuracy of the model was computed. Moreover, Fig. 21 illustrates the recognition results, indicating that the C-MvBLS model accurately identifies the coal and rock classes. The recognition results are generally consistent with the distribution of coal and rock in the roof. However, only index numbers 16 and 23 are misclassified. In addition, the overall recognition accuracy of the system was equal to 92.3 %, which demonstrates the system's effectiveness at the level of field applications.

Table 4
Distribution of coal and rock in the roof.

Color	Index	Class	Type	Color	Index	Class	Type
	1	Rock	Carbonaceous Mudstone		14	Rock	Sandy Mudstone
	2	Coal	Bituminous Coal		15	Coal	Bituminous Coal
	3	Rock	Carbonaceous Mudstone		16	Rock	Carbonaceous Mudstone
	4	Coal	Bituminous Coal		17	Coal	Bituminous Coal
	5	Rock	Mudstone		18		
	6	Coal	Bituminous Coal		19	Rock	Carbonaceous Mudstone
	7	Rock	Carbonaceous Mudstone		20		
	8	Coal	Bituminous Coal		21	Coal	Bituminous Coal
	9	Rock	Carbonaceous Mudstone		22	Rock	Carbonaceous Mudstone
	10				23	Coal	Bituminous Coal
	11	Coal	Bituminous Coal		24		Sandy Mudstone
	12				25	Rock	Siltstone
	13				26		Siltstone
					27		Gritstone

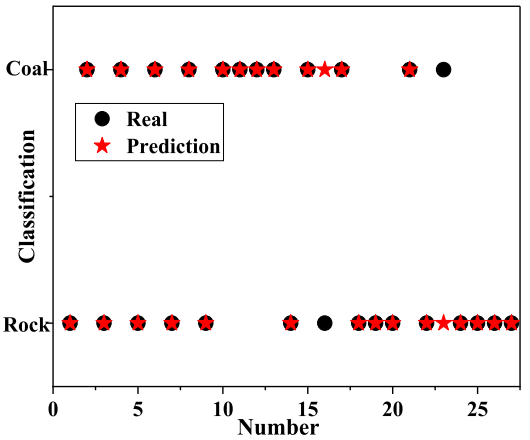

Fig. 21. Recognition result of two-classification.

6. Conclusion

During the LTCC, it is crucial to recognize different coal rock classes. To address this challenge, a field-deployable recognition system based on NIRS technology has been developed. It consists of two parts: the acquisition of light collection and the processing for recognition, this system is designed to detect different coal-rock classes during the roof coal caving process. Additionally, spectra under different influencing factors, such as granularity, light source angle, and detection sensor angle, are obtained to explain the potential effects and develop C-MvBLS model that eliminates them. The developed model applies a combination of convolution and multi-view features in a BLS structure to perform the two classifications for coal-rock samples with high accuracy rates reaching 99.78 %. Finally, the proposed recognition system with the model is deployed in real coal mines during the experiments, where the spectral data from a complete coal caving cycle is collected and classified with an accuracy rate of 92.3 % when considering two-classification.

However, this work still has some drawbacks, different types of coal and rock are present in the actual coal seam roof. In the feature processing stage, this method reduces the differences between various subtypes of rock and between different subtypes of coal, focusing primarily on the binary classification problem of coal and rock. However, when monitoring the material on the rear AFC, it is not possible to accurately determine the height of the coal seam from which the caved coal originated. Therefore, future work has been proposed, such as exploring fine-grained feature processing methods that can capture more subtle differences between subtypes, thereby improving the model's adaptability in complex environments. Based on this feature processing method, multi-class classification models could be introduced to consider more subtypes, enabling precise differentiation between different subtypes of coal and rock.

Data availability statement

All dataset have been deposited into the Zenodo, DOI: 10.5281/zenodo.8201508.

CRediT authorship contribution statement

Yuanbo Lv: Writing – review & editing, Writing – original draft, Visualization, Validation, Supervision, Software, Resources, Methodology, Formal analysis, Data curation, Conceptualization. **Shibo Wang:** Writing – review & editing, Project administration, Investigation, Funding acquisition, Conceptualization. **En Yang:** Software, Data curation.

Declaration of competing interest

The authors declare that they have no known competing financial interests or personal relationships that could have appeared to influence the work reported in this paper.

Acknowledgements

This work was supported in part by the projects of the Ministry of Industry and Information Technology under Grant TC220A04W-1/167,in part by the Scientific research projects of the Inner Mongolian under Grant 2022YFHH0007, in part by the National Key Research and Development Program of Shanxi under Grant 202102010101003 and in part by the Priority Academic Program Development (PAPD) of Jiangsu Higher Education Institutions.

References

[1] T.D. Le, R. Mitra, J. Oh, B. Hebblewhite, A review of cavability evaluation in longwall top coal caving, Int. J. Min. Sci. Technol. 27 (6) (2017) 907–915.
[2] W. Hongwei, W. Yongping, J. Jianqiang, C. Peipei, Stability mechanism and control technology for fully mechanized caving mining of steeply inclined extra-thick seams with variable angles, Mining, Metallurgy & Exploration 38 (2) (2021) 1047–1057.
[3] S. Jiulin, Z. Quntao, G. Xiaojin, X. Jisheng, Quantitative evaluation of top coal caving methods at the working face of extra-thick coal seams based on the random medium theory, Adv. Civ. Eng. 2021 (2021) 1–9.
[4] N. Zhang, C. Liu, X. Wu, T. Ren, Dynamic random arching in the flow field of top-coal caving mining, Energies 11 (5) (2018) 1106.
[5] S.S. Peng, F. Du, J. Cheng, Y. Li, Automation in U.S. longwall coal mining: a state-of-the-art review, Int. J. Min. Sci. Technol. 29 (2) (2019) 151–159.
[6] C. Liu, H. Li, Numerical simulation of realistic top coal caving intervals under different top coal thicknesses in longwall top coal caving working face, Sci. Rep.-UK 11 (1) (2021) 13254.
[7] X. Liu, W. Jing, M. Zhou, Y. Li, Multi-scale feature fusion for coal-rock recognition based on completed local binary pattern and convolution neural network, Entropy 21 (6) (2019) 622.
[8] M. Zhao, et al., Spatial Effect Analysis of Coal and Gangue Recognition Detector Based on Natural Gamma Ray Method, New York, N.Y, vol. 31, 2022, pp. 953–969, 2.
[9] Y.N. Pak, Z.S. Nuguzhinov, D.Y. Pak, M.O. Imanov, Neutron gamma-method for monitoring ash content of coal, atom, Energy 124 (3) (2018) 192–196.
[10] X. Zhou, X. Huang, P. Liu, T. Li, A probabilistic method to analyze collapse failure of shallow rectangular tunnels, Tunn. Undergr. Space Technol. 82 (2018) 9–19.
[11] H. Xiao-Cheng, W. Gui-Lin, C. Qiu-Nan, Z. Wei, Collapse failure assessment of geomaterials behind steel structure in tunnels using the Chebyshev inequalities, ASCE-ASME journal of risk and uncertainty in engineering systems, Part A: Civil Engineering 10 (3) (2024) 06024002.
[12] G. Wang, X. Huang, D. Bu, Z. Dai, How large is the collapsed area of ground collapse induced by tunnelling, Geomechanics and geoengineering, an international journal (2024) 1–14.
[13] H. Pang, et al., A feature extraction method using auditory nerve response for collapsing coal-gangue recognition, Appl. Sci. 10 (21) (2020) 7471.
[14] S.G. Zhu, G.H. Xue, X.Y. Zhao, E.M. Liu, M. Wu, Vibration signal time-domain characteristic extraction for coal and rock recognition at the fully mechanized top-coal caving face, ICMECT 556–562 (2014) 2862–2865.
[15] G. Zhang, Z. Wang, L. Zhao, Recognition of rock–coal interface in top coal caving through tail beam vibrations by using stacked sparse autoencoders, Journal of Vibroengineering 18 (7) (2016) 4261–4275.
[16] N. Zhang, C. Liu, Radiation characteristics of natural gamma-ray from coal and gangue for recognition in top coal caving, Sci. Rep.-UK 8 (1) (2018) 190.
[17] Y. Ozaki, Infrared spectroscopy-mid-infrared, near-infrared, and far-infrared/terahertz spectroscopy, Anal. Sci. 37 (9) (2021) 1193–1212.
[18] E.A. Cloutis, et al., Spectral reflectance "deconstruction" of the Murchison CM2 carbonaceous chondrite and implications for spectroscopic investigations of dark asteroids, Icarus 305 (2018) 203–224.
[19] P.A. Pinto, A.C.S.A. Anconi, L.R. de Abreu, E.J. Magalhães, C.A. Nunes, Strategies to determine lactose in cow milk by mid infrared spectroscopy, J. Food Compos. Anal. 104 (2021) 104176.
[20] B. Yang, et al., Identification of cumin and fennel from different regions based on generative adversarial networks and near infrared spectroscopy, Spectrochim. Acta Mol. Biomol. Spectrosc. 260 (2021) 119956.
[21] S. Bai, R. Nayar, J.F. Carpenter, M.C. Manning, Noninvasive determination of protein conformation in the solid state using near infrared (NIR) spectroscopy, J Pharm Sci 94 (9) (2005) 2030–2038.
[22] D. Xiao, T.T.G. Le, T.T. Doan, B.T. Le, Coal identification based on a deep network and reflectance spectroscopy, Spectrochim. Acta Mol. Biomol. Spectrosc. 270 (2022) 120859.
[23] D. He, B.T. Le, D. Xiao, Y. Mao, F. Shan, T.T.L. Ha, Coal mine area monitoring method by machine learning and multispectral remote sensing images, Infrared Phys. Techn. 103 (2019) 103070.
[24] L. Zou, X. Yu, M. Li, M. Lei, H. Yu, Nondestructive identification of coal and gangue via near-infrared spectroscopy based on improved broad learning, IEEE T. Instrum. Meas. 69 (10) (2020) 8043–8052.
[25] N. Begum, A. Maiti, D. Chakravarty, B.S. Das, Diffuse reflectance spectroscopy based rapid coal rank estimation: a machine learning enabled framework, Spectrochim. Acta Mol. Biomol. Spectrosc. 263 (2021) 120–150.
[26] X. Yu, W. Guo, N. Wu, L. Zou, M. Lei, Rapid discrimination of coal geographical origin via near-infrared spectroscopy combined with machine learning algorithms, Infrared Phys. Techn. 105 (2020) 103180.
[27] Y. Wang, M. Yang, G. Wei, R. Hu, Z. Luo, G. Li, Improved PLS regression based on SVM classification for rapid analysis of coal properties by near-infrared reflectance spectroscopy, Sensor. Actuator. B Chem. 193 (2014) 723–729.

[28] C.L.P. Chen, Z. Liu, Broad learning system: an effective and efficient incremental learning system without the need for deep architecture, IEEE Trans. Neural Netw. Learn. Syst. 29 (1) (2018) 10–24.
[29] J. Jin, C.L. Philip Chen, Regularized robust Broad Learning System for uncertain data modeling, Neurocomputing 322 (2018) 58–69.
[30] C.L.P. Chen, Z. Liu, S. Feng, Universal approximation capability of broad learning system and its structural variations, IEEE Trans. Neural Netw. Learn. Syst. 30 (4) (2019) 1191–1204.
[31] F. Yang, A CNN-based broad learning system, in: Proc. 2018 IEEE 4th International Conference on Computer and Communications, 2018.
[32] Y. Li, J. Jin, Y. Geng, Y. Xiao, J. Liang, C.L.P. Chen, Discriminative elastic-net broad learning systems for visual classification, Appl. Soft Comput. 155 (2024) 111445.
[33] J. Jin, B. Geng, Y. Li, J. Liang, Y. Xiao, C.L.P. Chen, Flexible label-induced manifold broad learning system for multiclass recognition, IEEE Trans. Neural Netw. Learn. Syst. (2023) 1–15.
[34] J. Jin, Z. Qin, D. Yu, Y. Li, J. Liang, C.L.P. Chen, Regularized discriminative broad learning system for image classification, Knowledge-Based Syst. 251 (2022) 109306.
[35] J. Jin, Y. Li, C.L.P. Chen, Pattern classification with corrupted labeling via robust broad learning system, IEEE Trans. Knowl. Data Eng. 34 (10) (2022) 4959–4971.
[36] T. Li, B. Fang, J. Qian, X. Wu, CNN-based broad learning system, in: Proc. 2019 IEEE 4th International Conference on Signal and Image Processing, 2019, pp. 132–136.
[37] Z. Shi, X. Chen, C. Zhao, H. He, V. Stuphorn, D. Wu, Multi-view broad learning system for primate oculomotor decision decoding, IEEE Trans. Neural Syst. Rehabil. Eng. 28 (9) (2020) 1908–1920.
[38] J. Zhao, X. Xie, X. Xu, S. Sun, Multi-view learning overview: recent progress and new challenges, Inf. Fusion 38 (2017) 43–54.
[39] R. Chen, et al., Carrier phase estimation of M-QAM based on cubic spline interpolation, Chin. J. Quant. Electron. (2023) 1–14.
[40] J. Luo, K. Ying, J. Bai, Savitzky–Golay smoothing and differentiation filter for even number data, Signal Process. 85 (7) (2005) 1429–1434.
[41] S. Baek, A. Park, Y. Ahn, J. Choo, Baseline correction using asymmetrically reweighted penalized least squares smoothing, The Analyst 140 (1) (2015) 250–257.
[42] H.G. R, V. R. K, The behavior of spectral features in the infrared emission from particulate surfaces of various grain sizes, J. Geophys. Res. 73 (18) (1968) 6039–6046.
[43] Y.X. Wang, J. Jian, L.G. Zhou, L.G. Hou, C. Wang, M. Cao, Mineral spectrum change analysis under the conditions of different particle, Size Spectroscopy and Spectral Analysis 35 (3) (2015) 803–808.
[44] C. Zhang, et al., Effect of granularity on the characteristics of visible-near infrared spectra of different coal particles, Spectroscopy and spectral analysis 42 (12) (2022) 3858–3863.